JGR Oceans

RESEARCH ARTICLE
10.1029/2018JC014227

Barotropic Kelvin Wave-Induced Bottom Boundary Layer Warming Along the West Antarctic Peninsula

D. J. Webb[1], R. M. Holmes[1,2], P. Spence[1], and M. H. England[1]

[1]ARC Centre of Excellence for Climate System Science, Climate Change Research Centre, University of New South Wales, Sydney, Australia, [2]School of Mathematics and Statistics, University of New South Wales, Sydney, Australia

Key Points:
- We examine the response of the Antarctic margin to East Antarctic wind anomalies based on an intensified southern annular mode
- Barotropic Kelvin waves propagate the signal around Antarctica, leading to changes in bottom stress, bottom Ekman transport, and near-bottom temperature
- We quantify model-simulated warming rates along the West Antarctic Peninsula that can be attributed to Kelvin wave-induced bottom Ekman flow under an idealized wind forcing scenario

Correspondence to:
D. J. Webb,
d.webb@unsw.edu.au

Citation:
Webb, D. J., Holmes, R. M., Spence, P., & England, M. H. (2019). Barotropic Kelvin wave-induced bottom boundary layer warming along the West Antarctic Peninsula. *Journal of Geophysical Research: Oceans*, *124*, 1595–1615. https://doi.org/10.1029/2018JC014227

Received 30 MAY 2018
Accepted 22 OCT 2018
Accepted article online 28 FEB 2019
Published online 10 MAR 2019

Abstract Intrusions of warm circumpolar deep water onto the Antarctic continental shelf are thought to drive accelerated loss of Antarctic glacial ice mass by triggering melt at the ice shelf grounding line. However, the mechanisms responsible for driving on-shelf circumpolar deep water intrusions are not well understood. Here we examine how sea surface height (SSH) anomalies propagating around the Antarctic coastline as coastal-trapped waves can drive warm water intrusions through changes in bottom Ekman transport. A wind perturbation motivated by the recent intensification and poleward shift of the southern annular mode during its positive phase is applied over Eastern Antarctica between 20°E and 120°E in two global ocean sea-ice models (1/4° and 1/10°) and a single-layer shallow water model. The changes in winds generate a drop in coastal SSH that propagates around Antarctica as a barotropic Kelvin wave. The SSH drop is accompanied by a barotropic flow, which alters the bottom stress, generating an onshore transport of warm water wherever thermal gradients are favorable. We estimate the resulting anomalous bottom Ekman flow and use temperature gradients calculated from the Southern Ocean State Estimate, along with the 1/4° and 1/10° models, to evaluate the resultant heat advection. We find that this mechanism can drive warming of up to 0.7 °C along the West Antarctic Peninsula within a year, depending on the mean state of the cross-shelf temperature gradient and the barotropic flow strength. Over longer time scales, warming eventually ceases due to saturation of the SSH field and arrest of the Ekman transport by buoyancy forces.

Plain Language Summary Antarctic glacial ice melt has accelerated in recent years, yet we still do not fully understand the mechanisms driving this increased melt. Part of the answer is thought to lie in intrusions of warm subsurface waters that come into contact with the base of Antarctica's ice shelves. However, the processes that drive these warm water intrusions are not yet well understood. Here we examine a mechanism for wind-driven changes in coastal sea level that propagate around Antarctica as coastal-trapped waves and consequently drive onshore heat transport via changes in bottom layer flow. We calculate an estimate for the warming rate associated with this mechanism using theory; model simulations; and, where available, observations. We further test the sensitivity of heat transport to local stratification as well as a parameter that determines the bottom flow strength. Each model simulation is forced with winds based on projections of an intensified westerly wind belt over the East Antarctic sector of the Southern Ocean. In each case we find substantial subsurface warming to develop along the West Antarctic Peninsula within 1 year, with the strongest warming seen where the net coastal flow, and the temperature gradients over the Antarctic continental shelf are greatest.

1. Introduction

The Antarctic ice sheets contain the majority of Earth's land-based ice mass and are potentially sensitive to changes in climate associated with atmospheric greenhouse gasses and ozone concentrations (Pritchard et al., 2012). Antarctic ice sheet and ice shelf melt is one of the biggest uncertainties in future projections of global sea level rise due to the poor representation of ocean-ice interactions and the uncertainty in how land-ice dynamics will respond to global warming (DeConto & Pollard, 2016). There is also considerable uncertainty in how warm water intrusions onto the Antarctic continental shelf will change in response to ongoing increases in anthropogenic forcing. This limited understanding motivates us to study the drivers of Antarctic ice shelf loss, and in particular the means by which off-shelf warm Circumpolar Deep Water (CDW) can be transported onto the shelf. Ice shelf melt around Antarctica is significantly enhanced by increases in oceanic subsurface temperatures (Depoorter et al., 2013; Hellmer et al., 2012) particularly along

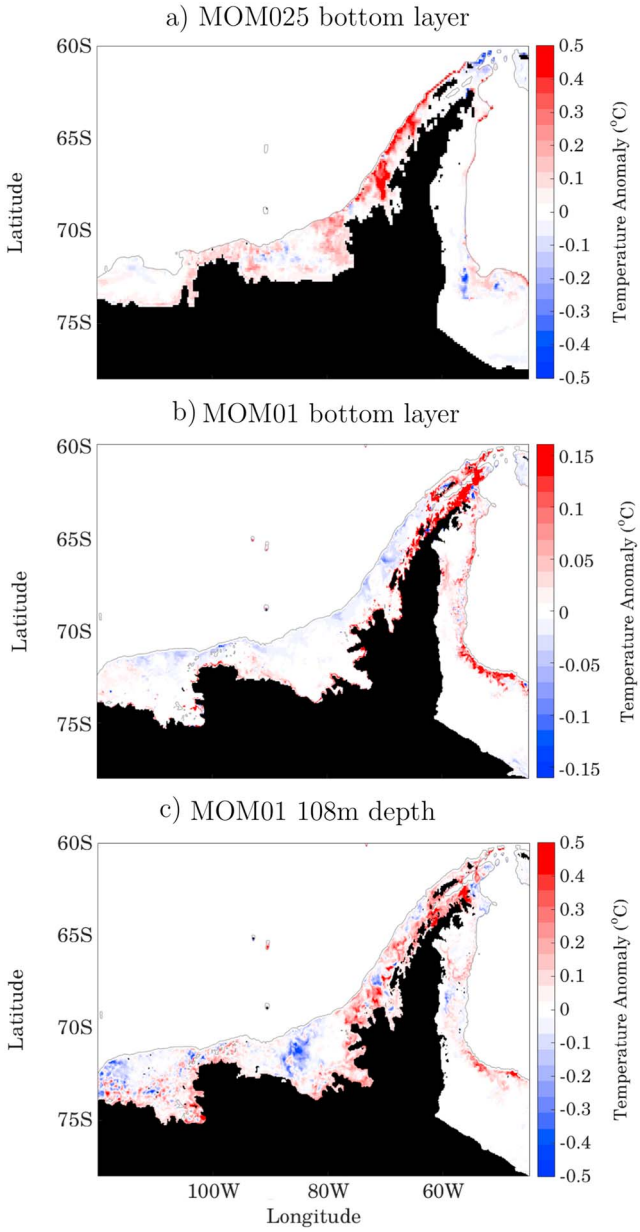

Figure 1. First year temperature anomalies (°C) along the West Antarctic Peninsula from the perturbation experiments of Spence et al. (2017) model output for (a) MOM025 bottom layer, (b) MOM01 bottom layer, and (c) MOM01 at 108-m depth. Thin gray line represents the 1,000-m isobath. Anomalies below 1,000 m are not shown.

the West Antarctic Peninsula where the rate of ice mass loss has doubled between 2003 and 2014 (Harig & Simon, 2015). Recent observations suggest that Antartic Continental Shelf Bottom Water is warming by ~0.1–0.3 °C/decade, particularly in the Amundsen and Bellinghausen Seas (Schmidtko et al., 2014). This is of concern as increases in subsurface ocean temperatures can significantly enhance the basal melt rate of ice shelves (Holland et al., 2008; Rignot et al., 2002). Thus, to accurately predict future ice sheet melt and global sea-level rise, we must understand the mechanisms responsible for oceanic subsurface warming around Antarctica.

The Antarctic Slope Front helps maintain a barrier between the warm waters of the Antarctic Circumpolar Current to the north and cold, fresh Antarctic coastal waters to the south (Jacobs, 1991). However, intrusions of CDW can cross the Antarctic Slope Front bringing warm and salty waters onto the continental shelf. There are a number of potential candidate mechanisms that can drive intrusions of CDW onto the Antarctic

continental shelf (Klinck & Dinniman, 2010). These include heat transport due to cross slope-front eddy fluxes, potentially active in regions along the continental shelf where density surfaces connect the continental shelf waters to offshore CDW. However, this generally corresponds to regions where the potential vorticity barrier associated with f/H gradients is weak, such as the Weddell Sea (Stewart & Thompson, 2015). Tides can also play a role by enhancing mixing and driving rectified cross-slope transport of CDW (Flexas et al., 2015; Robertson, 2013). Topography may also contribute by controlling the flow of warm water underneath the ice shelf (Jenkins et al., 2010; St-Laurent et al., 2013). Wind-stress curl changes over the continental shelf break have also been shown to alter cross-isobath ocean heat transport (Kimura et al., 2017; Rodriguez et al., 2016). Spence et al. (2014) have further shown that an observed poleward shift and strengthening of the Southern Hemisphere westerly winds (Thompson & Solomon, 2002) and subsequent shift in the polar easterlies can cause rapid subsurface warming due to a local-wind driven Ekman adjustment at the surface, which shoals isotherms. More recently, on-shelf bottom boundary transport of heat driven by coastal-trapped waves has been proposed as another factor at play (Spence et al., 2017). However, the relative role of each process and the interplay between these mechanisms remains unknown.

Many studies have shown that wind stress anomalies can drive sea-level variations around Antarctica (e.g., Aoki, 2002; Carrère & Lyard, 2003; Frankcombe et al., 2013). In turn, sea-level variations are known to drive variability in bottom Ekman transport and upwelling through changes in bottom stress (Cossu et al., 2010; Gill & Clarke, 1974). Spence et al. (2017) showed that changes in East Antarctic coastal winds can lead to rapid subsurface warming at locations remote from the wind changes, with a particularly strong response along the Western Antarctic Peninsula (WAP; see Figure 1). They suggest this is due to SSH anomalies propagating around Antarctica as barotropic Kelvin waves, which then alter the local temperature structure via a bottom Ekman layer response. However, they do not quantify the magnitude of bottom Ekman heat advection associated with this mechanism. Here we diagnose the range of simulated subsurface ocean warming that could be attributed to this mechanism by quantifying bottom layer heat advection anomalies using a range of model, reanalysis, and observational data.

To estimate the anomalous warming due to a barotropic velocity anomaly-induced bottom Ekman flow, we consider the response of the Antarctic circulation to a wind stress anomaly applied between 20°E and 120°E over East Antarctica, as studied by Spence et al. (2017). Locally, a westerly (easterly) wind stress anomaly will cause the SSH to be lowered (raised) along the shelf due to local offshore (onshore) surface Ekman transport. However, these SSH anomalies will also propagate along the coast away from the perturbation region as barotropic Kelvin waves. Barotropic Kelvin waves propagate around Antarctica at speeds of $\sqrt{gH}$ (where g is the gravitational acceleration and H is the ocean depth), enabling them to circumnavigate the entire Antarctic continent in approximately 1.5 days (Kusahara & Ohshima, 2014; Middleton et al., 1982), suggesting that even short time scale variability in coastal winds, of the order of several months, can affect remote locations, with SSH anomalies maturing over time scales of order 50 days (Spence et al., 2017). For a constant coastal wind perturbation, the generated Kelvin waves rapidly produce a circumpolar drop in SSH and an anomalous barotropic velocity field around the entire continent. The anomalous barotropic currents moving over the ocean floor then create a bottom stress anomaly, producing a bottom Ekman flow. This bottom Ekman flow can advect warm CDW onshore until the flow is arrested by buoyancy forces (Garrett et al., 1993; MacCready & Rhines, 1991). Taking into account this buoyancy-driven arrest, we will quantify the warming that can be attributed to the bottom Ekman adjustment to remotely generated SSH anomalies. We will also test the sensitivity of our results to different estimates of the Antarctic margin temperature field from observations and models, as well as to various Ekman layer depth parameters.

The remainder of this paper is divided as follows. In section 2 we derive an expression for the anomalous bottom Ekman velocity induced by a wind-driven (or otherwise) anomaly in the barotropic velocity field. We then go on to obtain approximate expressions for the temperature advection and subsequent temperature anomalies based on the derived bottom Ekman velocities and bottom temperature gradients. In section 3 we discuss the observations and model data we use to test the sensitivity of our calculation. The results, including bottom Ekman velocities, temperature gradients, Ekman arrest times, and temperature anomalies are presented in section 4. Finally, section 5 includes a discussion and summary of our findings.

2. Background and Theory

In this section we derive expressions for the response of the bottom Ekman layer to barotropic coastal circulation anomalies. Changes in coastal winds can result in SSH anomalies, and thus, changes in the barotropic coastal circulation that grow in time as barotropic Kelvin waves propagate around the continent. Changes in the barotropic circulation can then alter the turbulent bottom stress. This bottom stress can drive a bottom Ekman transport given by

$$\rho_0 \int_0^\infty \mathbf{u}_E dz = \frac{1}{f}\mathbf{F} \times \hat{\mathbf{z}}, \tag{1}$$

where ρ_0 is a reference density, $\mathbf{u}_E$ represents the velocity within the bottom Ekman layer, $\mathbf{F}$ is the bottom stress, and $\hat{\mathbf{z}}$ is the vertical unit vector. Here $z = 0$ refers to the ocean bottom. Assuming that the Ekman dynamics occurs within a distance of

$$\delta^* \equiv \delta A \tag{2}$$

off the bottom (which we will refer to as the *effective Ekman layer depth*), where δ is the theoretical bottom Ekman layer depth (equation (5)) and A is a dimensionless constant, which will be discussed shortly, we can express the bottom stress in terms of the average Ekman velocity in the effective bottom Ekman layer, $\bar{\mathbf{u}}_E$,

$$\rho_0 \delta^* \bar{\mathbf{u}}_E = \frac{1}{f}\mathbf{F} \times \hat{\mathbf{z}}. \tag{3}$$

The bottom stress, $\mathbf{F}$, can be derived using a quadratic stress law, $\mathbf{F} = \rho_0 C_d |\mathbf{U}|\mathbf{U}$, where C_d is the dimensionless drag coefficient and $\mathbf{U} = \mathbf{U_0} + \mathbf{U}'$ is the interior flow that generates the bottom stress, written as the sum of a mean flow, $\mathbf{U_0}$, and anomalous flow, $\mathbf{U}'$. Using equation (3), the average Ekman layer velocity can then be estimated as

$$\bar{\mathbf{u}}_E = \frac{C_d|\mathbf{U}|}{f\delta^*}\mathbf{U} \times \hat{z}. \tag{4}$$

Additionally, the theoretical Ekman layer depth, δ, is given by the ratio between bottom stress and Coriolis (e.g., Wåhlin & Walin, 2001)

$$\delta = C_d \frac{|\mathbf{U}|}{f}. \tag{5}$$

The anomalous bottom Ekman flow,

$$\bar{\mathbf{u}}'_E = \bar{\mathbf{u}}_E - \bar{\mathbf{u}}_{E,0} \tag{6}$$

(where $\bar{\mathbf{u}}_{E,0}$ is the bottom Ekman flow associated with the near-bottom mean flow $\mathbf{U_0}$), can then be obtained from equations (4) and (5),

$$\bar{\mathbf{u}}'_E = \frac{1}{A}\mathbf{U}' \times \hat{\mathbf{z}}. \tag{7}$$

Hence, the anomalous bottom Ekman flow is independent of the mean state. The anomalous bottom Ekman flow only depends linearly on the anomalous interior flow above the bottom boundary layer and the inverse of the effective thickness of the bottom Ekman layer depth parameterized by the constant A. This is a consequence of the form of δ since a change in the mean flow alters both the bottom stress and depth of the Ekman layer. The literature suggests (e.g., Cossu et al., 2010) that Ekman dynamics occurs over an effective Ekman layer thickness of $\sim \pi\delta$. For this reason $A = \pi$ would be a suitable choice, although we will examine the sensitivity of our results to this choice in section 4.8.

Over sloped bathymetry, the anomalous bottom Ekman velocity components are

$$\bar{u}'_E = \frac{V'}{A}\cos\theta_x, \tag{8}$$

$$\bar{v}'_E = -\frac{U'}{A}\cos\theta_y, \tag{9}$$

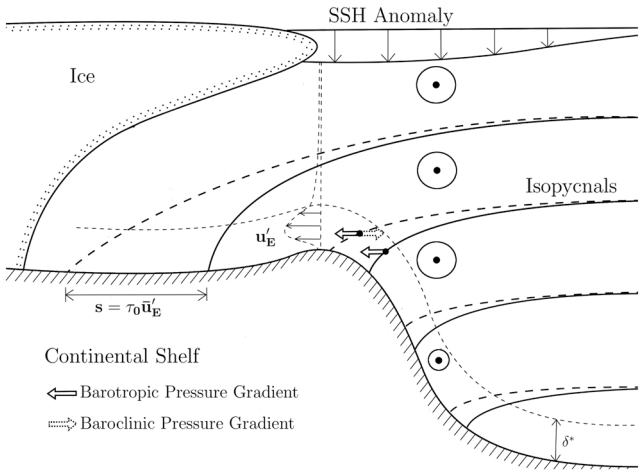

Figure 2. Schematic of the bottom Ekman flow mechanism discussed in this paper. Depressions in sea surface height (SSH) cause a barotropic pressure gradient toward the coast (thick solid arrows), which creates an anomalous geostrophic flow in the direction opposite to Kelvin wave propagation (circles with dots indicating flow out of page). The anomalous barotropic flow is slowed by bottom friction in the effective bottom Ekman layer of depth δ^* (indicated by the thin dashed lines), inducing an anomalous on-shore bottom Ekman flow, $\mathbf{u}'_E$, due to an imbalance between the pressure gradient and Coriolis force. The bottom Ekman flow shoals isopycnals (thick dashed lines) creating a baroclinic pressure gradient (dashed arrows), which increases until it balances the barotropic pressure gradient at which point the Ekman flow arrests.

$$\bar{w}'_E = \frac{1}{A}(V' \sin\theta_x - U' \sin\theta_y), \tag{10}$$

where $\theta_x \approx \partial H/\partial x$ and $\theta_y \approx \partial H/\partial y$ are the zonal and meridional bottom slopes, respectively, and U' and V' are the zonal and meridional components of the anomalous interior flow, $\mathbf{U}'$, in along-bottom coordinates (Cartesian coordinates rotated such that the positive z-axis is directed outward and perpendicular to the ocean floor). We will take U' and V' as barotropic, appropriate for the flows in our models. Once the anomalous bottom Ekman flow is established, it drives a cross-isobath temperature advection in the effective bottom Ekman layer given by

$$\left(\frac{\partial T}{\partial t}\right)_E = -\bar{\mathbf{u}}'_E \cdot \boldsymbol{\nabla} T, \tag{11}$$

where T is the background temperature. An anomalous bottom Ekman flow in the same direction as the temperature gradient (i.e., down the temperature gradient) gives rise to local cooling.

Anomalous flow continues to drive temperature advection until it is arrested by the development of internal buoyancy forces (see Figure 2). The changes in the near-bottom density field, brought about by the Ekman layer advection of density, lead to a baroclinic pressure gradient with associated thermal wind shear that reduces the bottom stress caused by the barotropic flow and thus reduces the anomalous bottom Ekman flow. The time scale over which this occurs is known as the Ekman arrest time (Brink & Lentz, 2010; MacCready & Rhines, 1993; Wåhlin et al., 2012); for a review on the subject see Garrett et al. (1993). As shown by MacCready and Rhines (1993), an estimate for the Ekman layer arrest time, τ_0, for a constant anomalous flow is

$$\tau_0 = \frac{f}{(N\alpha)^2}, \tag{12}$$

where α is the bottom slope in the direction of advection (θ_x or θ_y in the zonal and meridional directions, respectively) and N is the Brunt-Väisälä frequency based on the background stratification. We can thus estimate that isopycnals will be displaced along the bottom by a distance $\mathbf{s} \approx \tau_0 \bar{\mathbf{u}}'_E$ (see Figure 2).

For a steady flow, we can estimate the temperature anomaly at a given time by the minimum of accumulated time, t, and the Ekman arrest time, multiplied by the temperature advection, that is,

$$\Delta T(\mathbf{x}, t) = \left(\frac{\partial T(\mathbf{x})}{\partial t}\right)_E \min(t, \tau_0(x, y)). \tag{13}$$

For a nonsteady flow, the bottom Ekman velocity continually decreases as the baroclinic pressure gradient increases. This behavior leads to an exponential decay of advection rather than an instant shutoff at the Ekman arrest time. However, since the time integral of an exponential curve is equal to its decay scale (i.e., the arrest time), we do not expect this difference to be large. In general, the anomalous flow is continually varying, which also complicates the simple shutoff scheme. Temperature advection thus depends on the change in flow over each time interval and varies spatially due to the distribution of anomalous flow, temperature gradients, and the dependence of the Ekman arrest time on bottom slope and stratification. In general, the temperature anomaly is given by the integral of equation (11),

$$\Delta T(\mathbf{x}, t) = -\int_0^t \bar{\mathbf{u}}'_E \cdot \boldsymbol{\nabla} T dt'. \tag{14}$$

For the details of how we numerically evaluate the temperature anomaly see Appendix A.

Table 1
Summary of reanalyses and models used to derive estimates of warming due to the bottom boundary layer advective mechanism

Reanalyses and models used to derive bottom boundary layer advective warming			
	$\mathbf{u}_{BT\,\text{model}}$	u_{MOM025}	u_{MOM01}
T_{SOSE}	BT-SOSE	MOM025-SOSE	MOM01-SOSE
T_{MOM025}	BT-MOM025	MOM025-MOM025	-
T_{MOM01}	BT-MOM01	-	MOM01-MOM01

Note. MOM025 and MOM01 refer to the 1/4° and 1/10° Modular Ocean Model (MOM) simulations respectively. BT refers to the barotropic single-layer shallow water model, and SOSE is the Southern Ocean State Estimate.

3. Models and Data

In order to understand the contribution of remote coastal wind anomalies to shelf water warming via bottom Ekman transport, we use the anomalous barotropic velocity fields of the Spence et al. (2017) perturbation experiments to calculate bottom Ekman velocities (using equation (7)) from each model. The models include a single-layer shallow water model (at 1/4° resolution) as well as two ocean-sea ice runs, one at 1/4° and the other at 1/10° resolution. The calculated bottom Ekman velocities are then interpolated onto several different climatological/model background temperature fields (used to calculate the temperature gradients, ∇T, in equation (11)), allowing us to estimate the spatially dependent temperature advection, Ekman arrest time, and total warming anomaly in each case. Using several models for the anomalous velocity fields, and models, a reanalysis product and direct observations for the temperature gradients, we perform a sensitivity study on the warming associated with the Kelvin wave—bottom Ekman layer mechanism on model grid resolution and mean state bias.

3.1. Model Descriptions

We will examine the experiments of Spence et al. (2017) wherein positive southern annular mode (SAM) wind perturbations are applied only along the East Antarctic coastline between 20°E and 120°E. Two Modular Ocean Model (MOM5; Griffies, 2016) configurations are used: one with 1/4° horizontal resolution (50 vertical levels) and one with 1/10° horizontal resolution (75 vertical levels). These model configurations are referred to as MOM025 and MOM01, respectively. A single-layer shallow water model configured using the Regional Ocean Modeling System (Shchepetkin & McWilliams, 2005) at 1/4° resolution, which we will refer to as the BT (barotropic) model, is used to isolate only barotropic dynamics. Each model contains bottom friction parameterized by a spatially dependent quadratic drag coefficient, C_d (varying between 4 and 7×10^{-3} on the continental slope). All model configurations use the etopo5 bathymetry data set and have identical wind forcing based on the East Antarctic wind anomaly scenario of Spence et al. (2017), wherein wind perturbations are initiated from 200-year (MOM025) and 50-year (MOM01) long control state simulations using atmospheric forcing from CORE-NYF. We use the ETOPO5 bathymetry to remain consistent with Spence et al. (2017); however, it is worth noting that uncertainties in the bathymetry remain significant (e.g., Nitsche et al., 2017), and improvements are needed for more realistic quantifications of bottom boundary processes, such as those studied here. We consider only the first year, and the BT model is forced by only the anomalous forcing. See Spence et al. (2017) for more information on the model configurations and perturbation experiments.

3.2. Velocity Fields

Barotropic velocity anomaly fields are obtained for MOM025 and MOM01 by taking the difference between the 10-member ensemble averages of the wind forced and control simulations. Five-daily averaged barotropic velocity anomalies were then used to calculate the approximate anomalous bottom Ekman velocity fields using equation (7). The results were tested using daily averaged velocities in place of 5-daily averaged velocities, and there was little difference in the final result. We use the barotropic velocities, as the model velocity fields remain largely barotropic over the period of interest (see section 4.1).

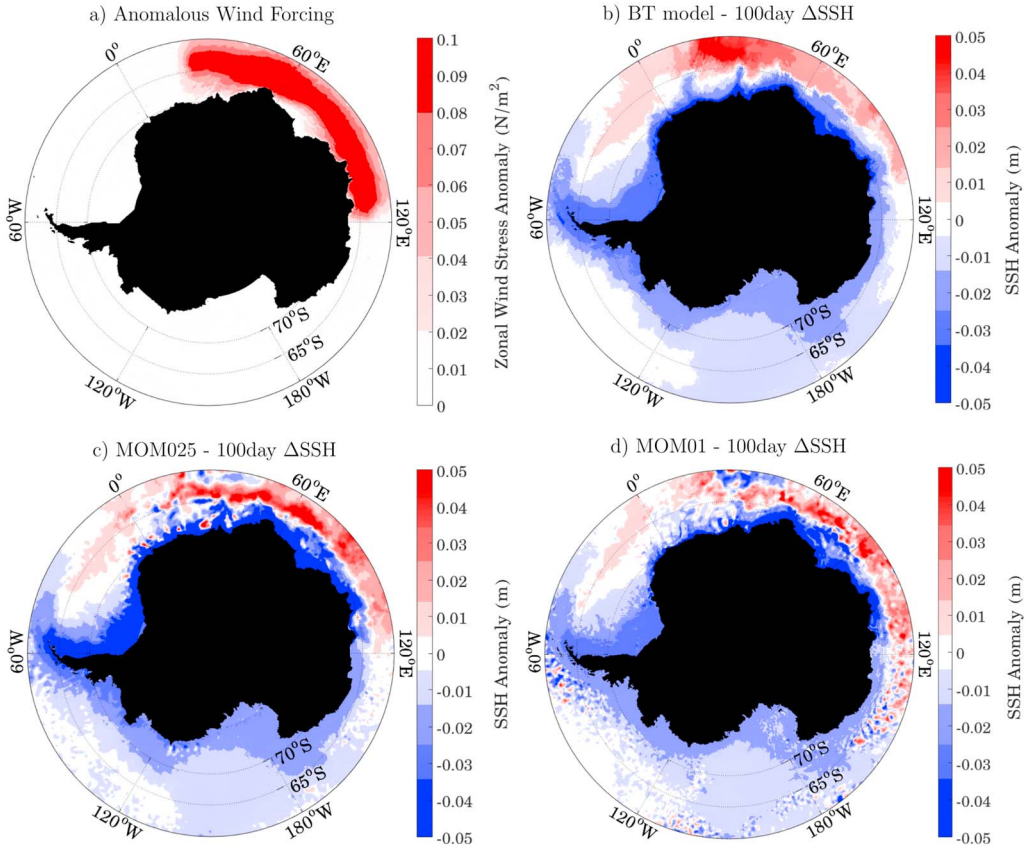

Figure 3. (a) Anomalous wind stress applied as a constant surface forcing anomaly to all models. Sea surface height anomalies after 100 days of anomalous wind forcing for (b) BT model, (c) MOM025, and (d) MOM01. BT = barotropic; MOM = Modular Ocean Model.

3.3. Temperature, Density, and Bathymetry Data

Potential temperature and density fields from MOM025, MOM01, and the Southern Ocean State Estimate (SOSE; Mazloff et al., 2010) are used to estimate the background temperature gradient and stratification in each case, that is, for ∇T in equation (11) and N^2 in equation (12). We use the annual mean temperature and density fields from the long term average of SOSE (version 2) and the annual mean of the ensemble average for MOM025 and MOM01 simulations; thus, the effects of the seasonal cycle in subsurface shelf water temperature have not been evaluated. The bathymetric slope is calculated from the model grid bathymetry within the same model from which the model velocity fields are obtained.

3.4. Summary of Cases

To evaluate the sensitivity of our results to bottom Ekman velocities and the background temperature gradient, we examine seven cases, comprising a combination of model and reanalysis fields of velocity and temperature. These cases are denoted by the velocity configuration followed by the climatological temperature (and density) distribution, T, used (SOSE or model), namely, BT-SOSE, BT-MOM025, BT-MOM01, MOM025-SOSE, MOM025-MOM025, MOM01-SOSE, and MOM01-MOM01 (see Table 1).

4. Results

4.1. Sea Surface Height and Barotropic Velocity

The wind stress anomaly applied over the ocean region next to East Antarctica (Figure 3a) generates a circumpolar SSH drop with accompanying along-isobath barotropic velocities in the direction opposite to Kelvin wave propagation (generally eastward along the coastline; Figures 3b–3d and 4; see Spence et al., 2017, Figure 3 for Hovmöller diagrams showing Kelvin wave propagation). After 1 year of anomalous wind forcing, the MOM025 anomalous velocity field remains almost completely barotropic except between 0°E and 120°E, approximately where the wind perturbation is applied. The MOM01 anomalous velocity field

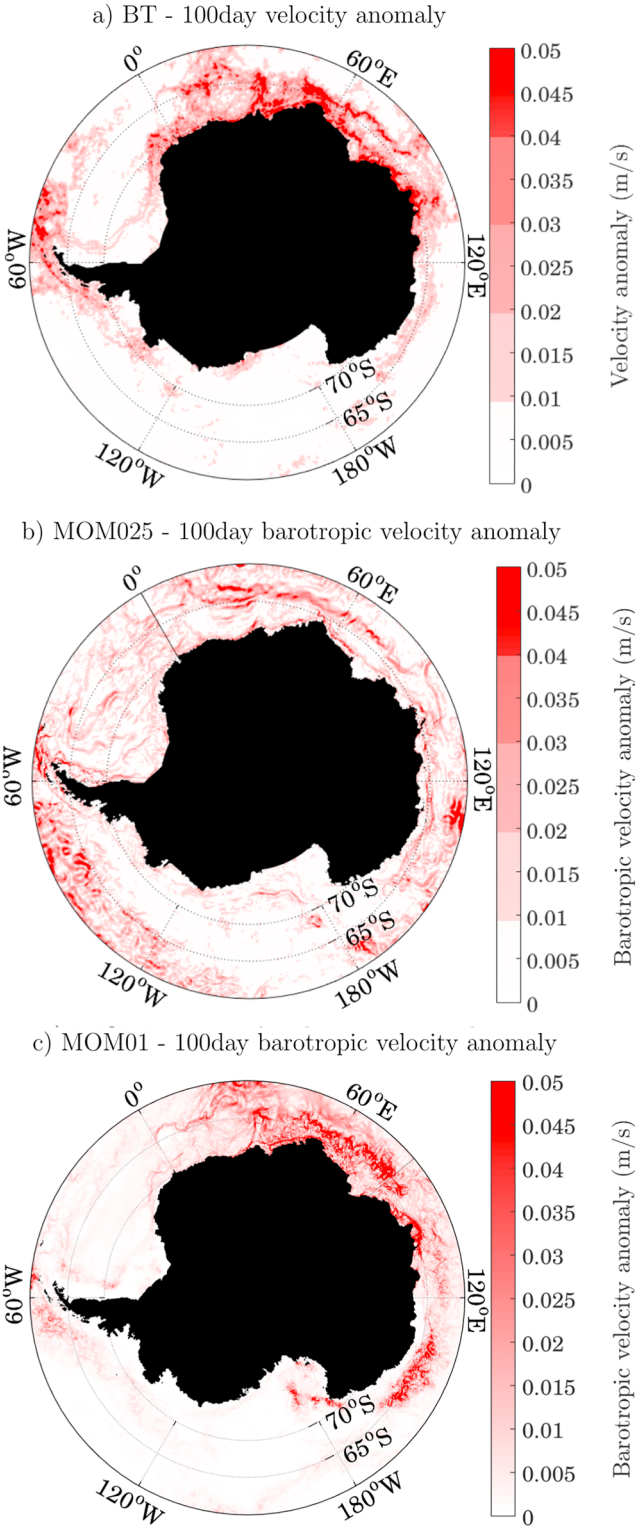

Figure 4. Five-day snapshot of the barotropic velocity anomaly magnitude (m/s) after 100 days of anomalous wind forcing over East Antarctica for (a) BT model, (b) MOM025, and (c) MOM01. BT = barotropic; MOM = Modular Ocean Model.

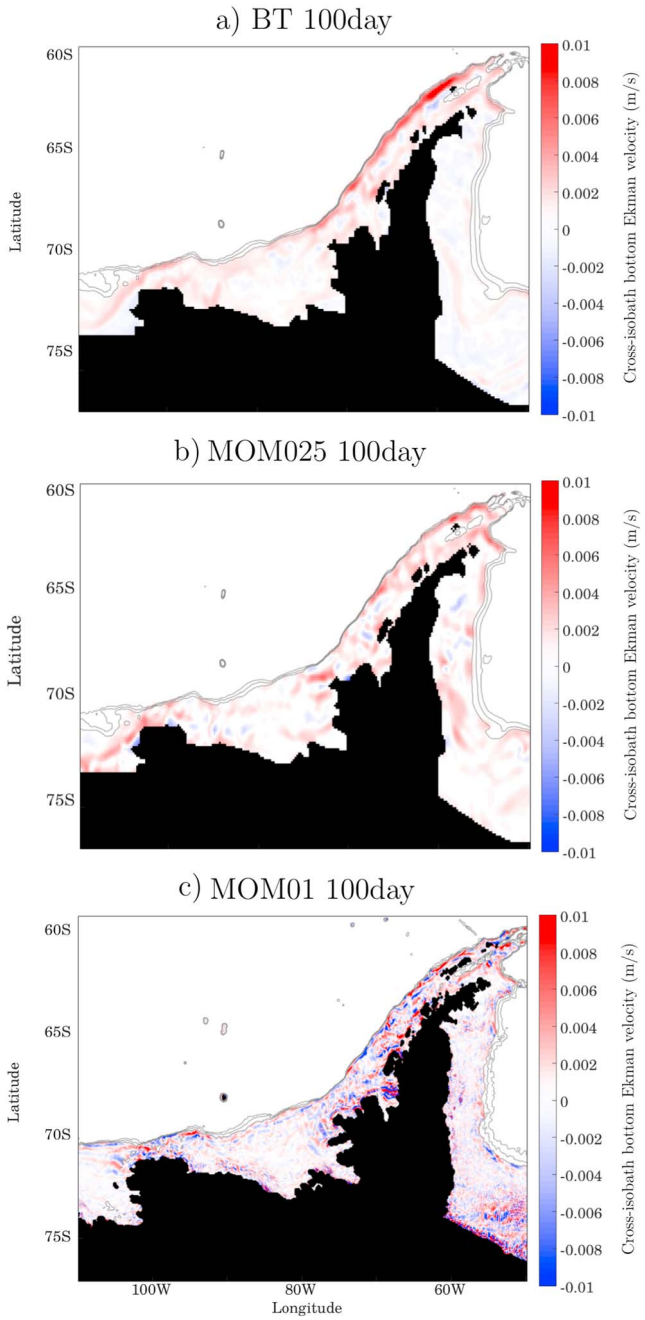

Figure 5. Five-day snapshot of the cross-isobath component of the bottom Ekman velocity field (m/s) along the West Antarctic Peninsula section after 100 days of wind anomalous forcing over East Antarctica for (a) BT model, (b) MOM025, and (c) MOM010. Red (positive values) indicates an upslope flow. Gray lines show 500-, 1,000-, and 1,500-m isobaths. Velocity anomalies below 1,000 m are not shown. BT = barotropic; MOM = Modular Ocean Model.

has a larger baroclinic component; the flow however remains largely barotropic (up to 0.05 m/s in magnitude) along West Antarctica away from the wind forced region (Figure 4c). This justifies using the barotropic velocity anomaly for $\mathbf{U}'$ in equation (7). In each case the generated flow is in the direction opposite to Kelvin wave propagation along the coast and concentrated along steep regions of the continental slope where f/H contours converge. The spatial structure of this anomalous barotropic flow sets the distribution of the upslope bottom Ekman velocity (Figure 5; discussed in the following section) which, in conjunction with stratification, determines the spatial structure of the subsurface warming response.

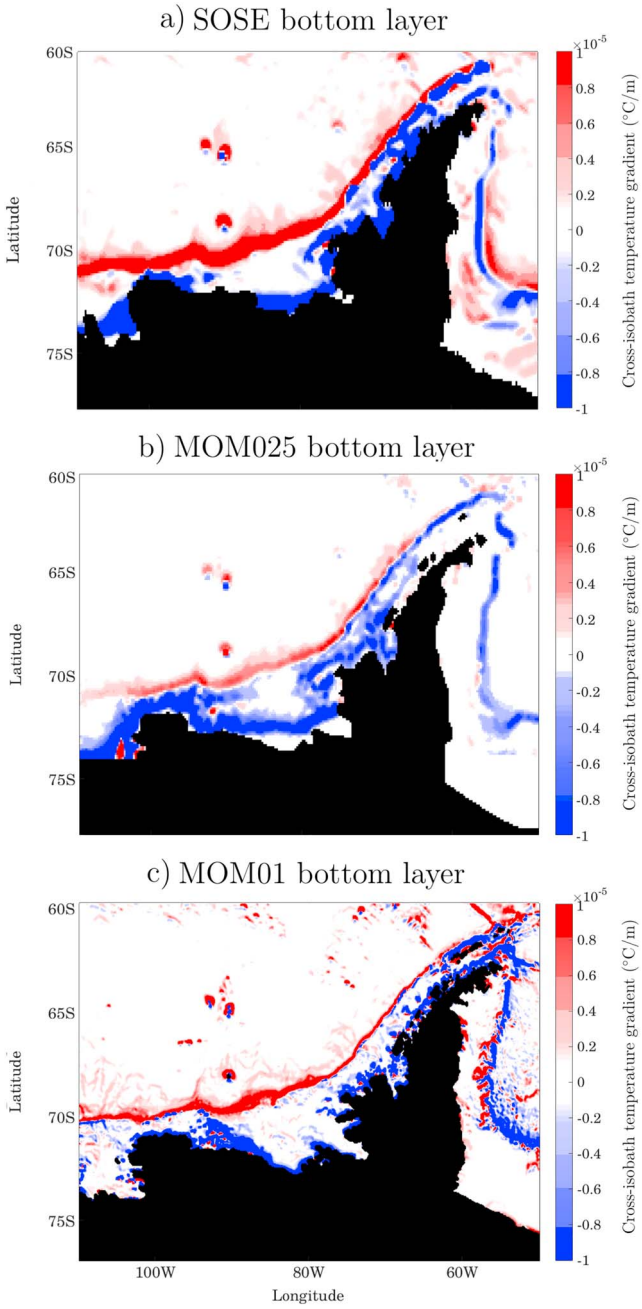

Figure 6. Cross-isobath component of the temperature gradients (°C/m) along the West Antarctic Peninsula for (a) SOSE, (b) MOM025, and (c) MOM010. SOSE temperature gradients were calculated from the annual mean of the long term average. MOM025 and MOM01 temperature gradients were calculated from the annual mean of the control run. Blue indicates bottom layer temperatures increasing downslope (i.e., with depth). BT = barotropic; MOM = Modular Ocean Model; SOSE = Southern Ocean State Estimate.

4.2. Bottom Ekman Velocity

The anomalous SSH-driven barotropic velocity fields generate bottom stress anomalies that drive an anomalous cross-isobath bottom Ekman flow. After 1 year, each model configuration shows the anomalous bottom Ekman velocity to be directed generally upslope and concentrated along the Antarctic continental slope where the barotropic flow is focused (Figure 5). In particular, the WAP shows a strong onshore bottom Ekman velocity in close proximity to the Antarctic shelf due to the steep continental slope. This is most clearly seen in the BT model. It is also seen in MOM025 and MOM01, but there are also downslope

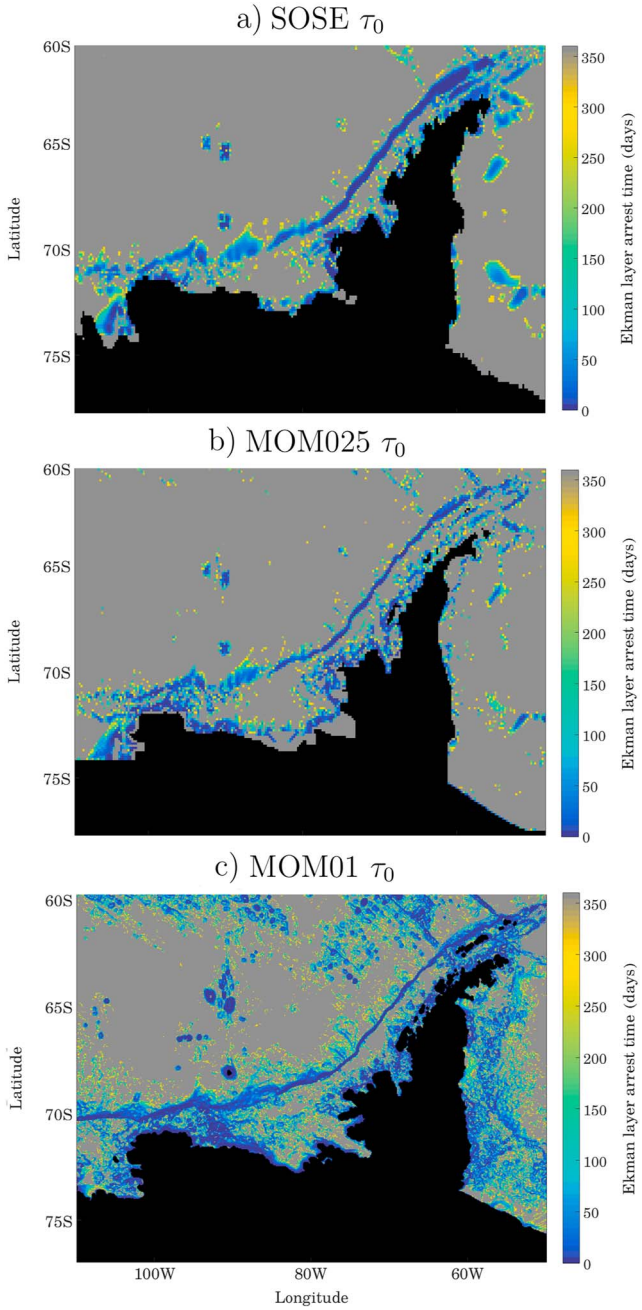

Figure 7. Ekman layer arrest time, τ_0 (equation (12)), for (a) SOSE, (b) MOM025, and (c) MOM010. Arrest times are calculated using the model grid bathymetry and density fields from the annual mean of the control run. MOM = Modular Ocean Model; SOSE = Southern Ocean State Estimate.

components to the bottom Ekman velocity due to mesoscale time-mean features, which are not completely removed by the ensemble average.

4.3. Temperature Gradients

Anomalous temperature advection in the effective bottom Ekman layer depends on both the bottom Ekman velocities described above and the temperature gradient in the bottom layer. All temperature gradients in the bottom layer show cooler temperatures toward shore on the continental shelf and upper slope (blue in Figure 6). On the deeper parts of the Antarctic continental slope, the water cools with depth (red in Figure 6). SOSE, MOM025, and MOM01 temperature gradients show similar features, the key differences between

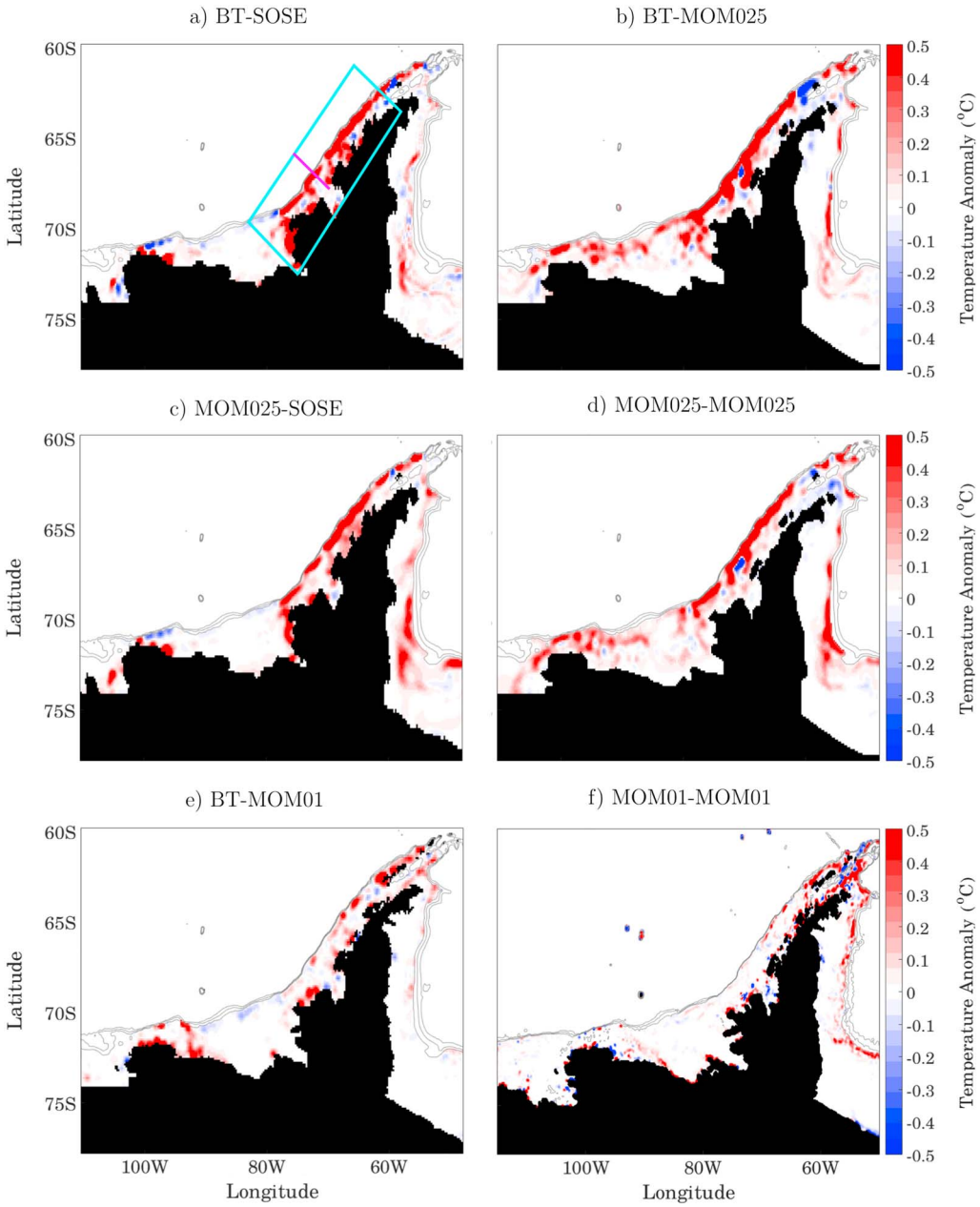

Figure 8. First year temperature anomalies (°C) for BT model velocity field advecting the (a) SOSE, (b) MOM025, and (e) MOM01 temperature fields; MOM025 velocity fields advecting the (c) SOSE and (d) MOM025 temperature fields; and (f) MOM010 velocity fields advecting the MOM010 temperature field. Gray lines show 500-, 1,000, and 1,500-m isobaths. The Western Antarctic Peninsula region over which temperature anomalies are averaged in Figure 10 is outlined by the light blue rectangle. The solid purple line indicates the WOCE S04P line data available in this region (used in Figure 11). BT = barotropic; MOM = Modular Ocean Model; SOSE = Southern Ocean State Estimate; WOCE = World Ocean Circulation Experiment.

them being their distance and extent from the Antarctic coastline, which can affect the location of advected warming. SOSE and MOM01 temperature gradients along the WAP are most negative (i.e., conducive to warming with an onshore flow) close to the coastal boundary. However, the SOSE offshore warming gradients have a larger spatial extent on the continental shelf so we expect warming to be more widespread with the SOSE temperature structure than MOM01. MOM025 has a similar spatial structure to SOSE however the negative cross-isobath temperature gradients (i.e., temperatures increasing with depth) on the continental shelf are located further from the coast in MOM025 relative to SOSE.

4.4. Ekman Arrest Times

The advection of tracer gradients in the bottom boundary layer continues until internal buoyancy forces arrest the flow, over a period given by the Ekman arrest time. We find the Ekman arrest time (equation (12)) to be shortest (hours to days) along the continental slope and coastline where there is stronger stratification and a steeper slope (Figure 7). Longer arrest times (up to a year) are present on the continental shelf where the bathymetry is relatively flat, allowing advection over the continental shelf to continue relatively uninhibited. The arrest times are relatively consistent between cases: hours to days along the slope and months to years off the slope.

4.5. Estimated Bottom Layer Warming

Using the bottom layer Ekman velocities, the temperature gradients, and the Ekman arrest times to calculate the temperature anomalies, we find warming in each configuration, particularly along the WAP between 80° W and 60° W, where the average temperature increase is approximately 0.1–0.7°C (from MOM01-MOM01 to BT-MOM025 using $A = \pi$) over 1 year (Figures 8 –10). The combination of strong onshore bottom Ekman transports along the continental slope at close proximity to strong along bottom temperature gradients allows significant advection of warm CDW onto the continental shelf. Although we are most interested in the warming signal along the WAP, we also find anomalous warming along other regions of the Antarctic continental slope for BT and MOM025; for example, consistent warming is seen near the shelf break between the Amundsen and Ross Seas (Figure 9; 130° W–160° W). Focusing on the warming averaged over a region of the WAP (blue region in Figures 8a and 9), we find warming to be the strongest when estimated using the BT model velocities combined with the MOM025 temperature field, and the weakest when estimated using the MOM01 flow fields and temperature gradients. Regardless of the magnitude of warming, we find the effective bottom Ekman layer temperature anomaly to steadily increase over the first year (Figure 10).

4.6. Sensitivity to Estimates of u_{Ek}

The velocity fields from the BT model produce the most warming since (unlike MOM025 and MOM01) there is no loss of barotropic energy into baroclinic processes in the ocean interior. This translates to stronger onshore bottom Ekman velocities leading to a stronger advective warming signal (compare Figure 10a with Figures 10b and 10c; note the differing y-axis scales). The anomalous barotropic flow continuously increases in the first year driving a steady increase in the temperature anomaly over the first year, which then begins to saturate as the SSH anomaly stabilizes. For the BT model, this effect dominates the anomalous temperature trend (Figure 10a). In contrast, the velocity fields in MOM025 and MOM01 are disturbed by baroclinic processes and mesoscale features such as eddies and flow meanders, which are not completely removed by our ensemble average. This can produce transient westward barotropic velocity anomalies, which lead to localized downslope bottom Ekman velocities, correlated with mesoscale activity seen in the anomalous SSH field. Thus, short periods of cooling or reduced warming can appear in the evolution of the temperature anomalies for the MOM025 and MOM01 velocity configurations (Figures 10b and 10c).

4.7. Sensitivity to Estimates of ∇T and τ_0

The temperature anomalies calculated for the bottom Ekman advective transport exhibit a strong spatial correlation with the background temperature gradients (compare Figures 6 and 8); the stronger the upslope thermal gradient, the more rapid the warming. The BT-SOSE configuration shows the average warming along the WAP exceeding 0.5 °C in the first year (Figure 10a; also see Figures 8a and 9a). By replacing the SOSE climatology with MOM025 and MOM010, we find the location of warming to be redistributed according to the magnitude of the offshore temperature gradients and Ekman arrest time fields (Figure 8). In BT-MOM025 the anomalous warming signal increases, whereas BT-MOM01 shows a decrease in the total temperature anomaly compared to BT-SOSE (Figure 10a). This behavior (warming greatest when calculated using the MOM025 temperature fields, followed by SOSE, then MOM01) is also obtained when using the MOM025 and MOM010 velocity fields (not shown). However, there is an exception with MOM025-MOM025 and MOM025-SOSE (black and red solid lines in Figure 10b), where stronger warming anomalies are obtained when using the SOSE temperature climatology. This exception is due to the MOM025 velocity fields being more spatially correlated with SOSE than the MOM025 temperature gradients along the WAP, but the differences are minor.

Comparing the warming due to the bottom Ekman layer advection mechanism to the actual bottom layer temperature anomalies from the MOM025 and MOM01 perturbation experiments (Figure 1) allows us to

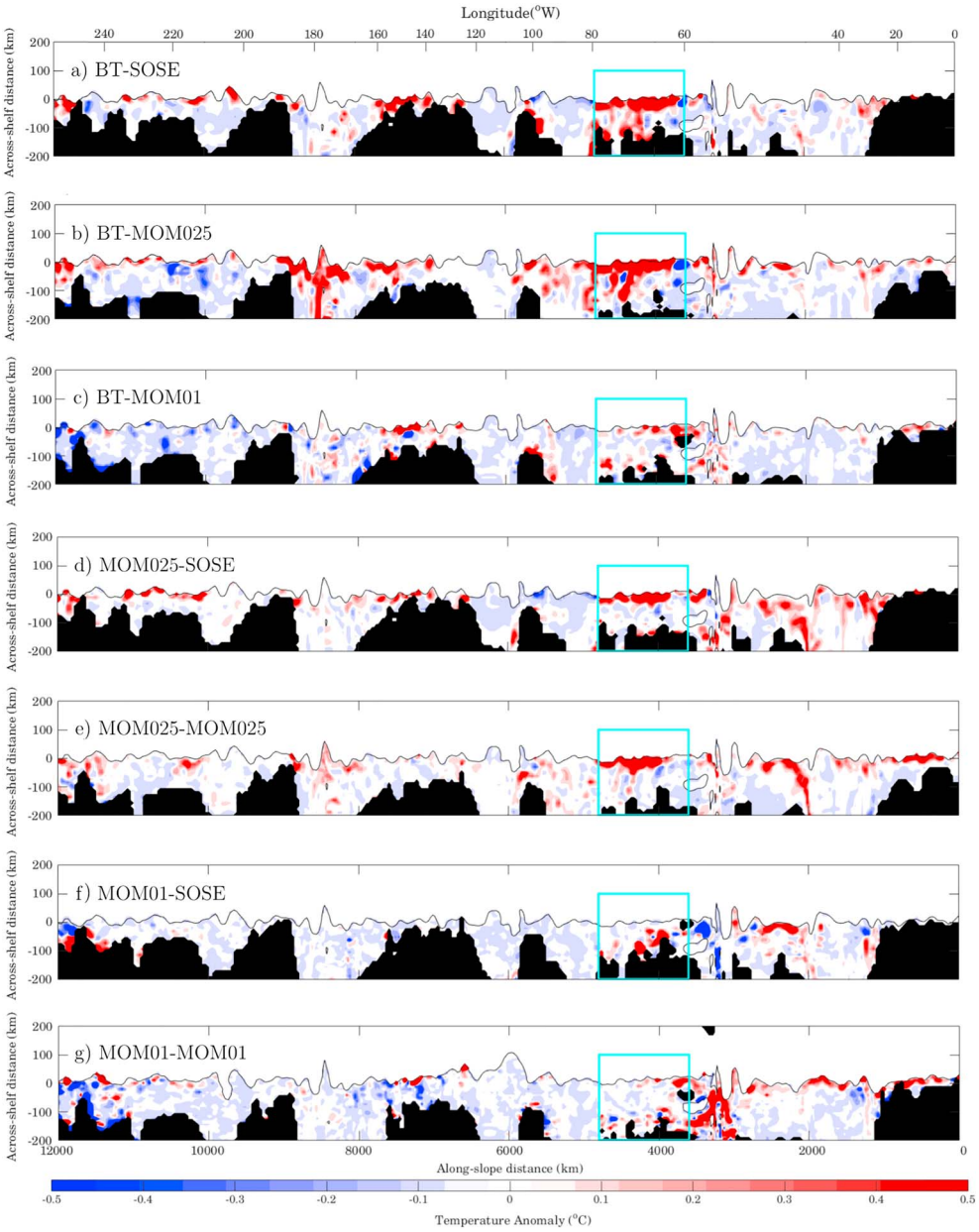

Figure 9. First year temperature anomalies (°C) in a cross- and along- isobath coordinate system. Across-shelf profiles are plotted relative to a smoothed (over a scale of roughly 350 km) 1,000-m isobath, which defines the across-shelf distance 0 km. The wind forced region (20–120°E), where warming is dominated by wind-driven Ekman transport, is not shown. Temperature anomalies are shown at <1,000-m depth (before smoothing) for BT velocity field advecting the (a) SOSE, (b) MOM025, and (c) MOM010 temperature fields. MOM025 velocity fields advecting the (d) SOSE, and (e) MOM025 temperature fields, and MOM01 velocities advecting the (f) SOSE and (g) MOM010 temperature fields. The thin black line represents the (nonsmoothed) 1,000-m isobath. The Western Antarctic Peninsula peninsula region considered for temperature anomaly averaging (used in Figure 10) is outlined by the light blue rectangle. BT = barotropic; MOM = Modular Ocean Model; SOSE = Southern Ocean State Estimate.

gauge the importance of the bottom Ekman-Kelvin wave mechanism first proposed by Spence et al. (2017) (compare solid and dashed lines in Figures 10b and 10c). The diagnostic temperature anomaly in MOM025 follows the same trend as the actual temperature anomaly, increasing rapidly for the first 6 months of wind forcing and then slowing. However, the magnitude of the actual model warming is a factor of approximately 3 less than the diagnosed warming due to the Kelvin wave-bottom Ekman layer advection mechanism. We discuss possible reasons for this difference in section 4.9.

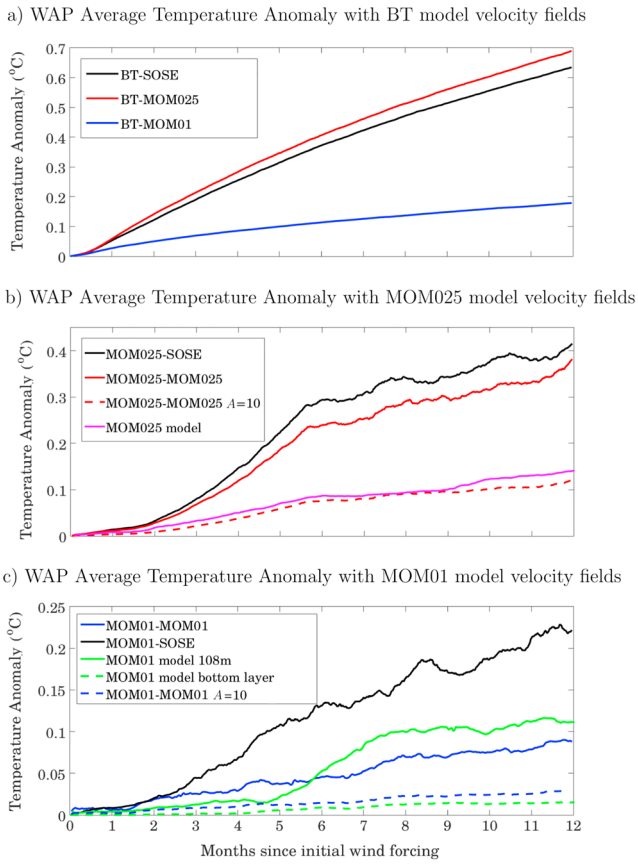

Figure 10. Evolution of average temperature anomalies along WAP sections between 60°W and 80°W above the 1,000-m isobath (see blue region in Figures 8a and 9) for (a) BT model velocity fields advecting the temperature fields from SOSE (black), MOM025 (red), and MOM01 (blue); (b) MOM025 velocities advecting the SOSE (black) and MOM025 (solid red) temperature fields. The red dashed line shows the temperature anomaly when the Ekman layer is scaled as $\delta^* = 10\delta$ (i.e., $A = 10$), instead of $\delta^* = \pi\delta$. The purple line indicates the actual temperature anomalies in the bottom layer from the MOM025 model output. Finally, (c) shows MOM01 velocities advecting the SOSE (black) and MOM01 (blue) temperature fields, and actual temperature anomalies from the MOM01 model output (green). The green dashed line shows the actual MOM01 temperature in the bottom layer and the green solid line is at 108-m depth. BT = barotropic; MOM = Modular Ocean Model; SOSE = Southern Ocean State Estimate; WAP = Western Antarctic Peninsula.

4.8. Sensitivity to Velocity and Stratification Coherence

Warming trends in MOM01-SOSE, MOM025-SOSE, and BT-SOSE reach 0.2, 0.4, and 0.6 °C, respectively, along the WAP within 1 year. With the temperature fields fixed to SOSE, disparity between the estimates is due to differences in the barotropic velocity fields and their correlation with the SOSE temperature gradients. Comparison of the bottom Ekman velocities (Figure 5), which all show similar spatial patterns on the shelf, to the bottom-layer SOSE temperature gradients (Figure 6a), suggests that the majority of this warming difference is due to the barotropic velocity strength. The BT model exhibits the largest magnitude barotropic velocity anomalies in the WAP region (Figure 4), followed by MOM025 and MOM01.

4.9. Sensitivity to the Effective Ekman Layer Depth

The calculated temperature anomaly scales directly with the choice of our parameter A introduced in equation (2). Since the Ekman transport is set by the anomalous barotropic flow, adjusting the effective Ekman layer depth by increasing (decreasing) A causes the bottom Ekman velocity anomaly to decrease (increase). This reduction (enhancement) of the bottom Ekman velocity reduces (enhances) temperature advection across the continental slope. Our main results assume $A = \pi$, corresponding to effective Ekman layer depths of 12–22 m over the slope. However, choosing $A = 10$, corresponding to an effective Ekman layer depth of 40–70 m along the continental slope, gives us results consistent with the model output from both MOM025 and MOM01 (compare dashed and solid lines in Figures 10b and 10c). This agreement is

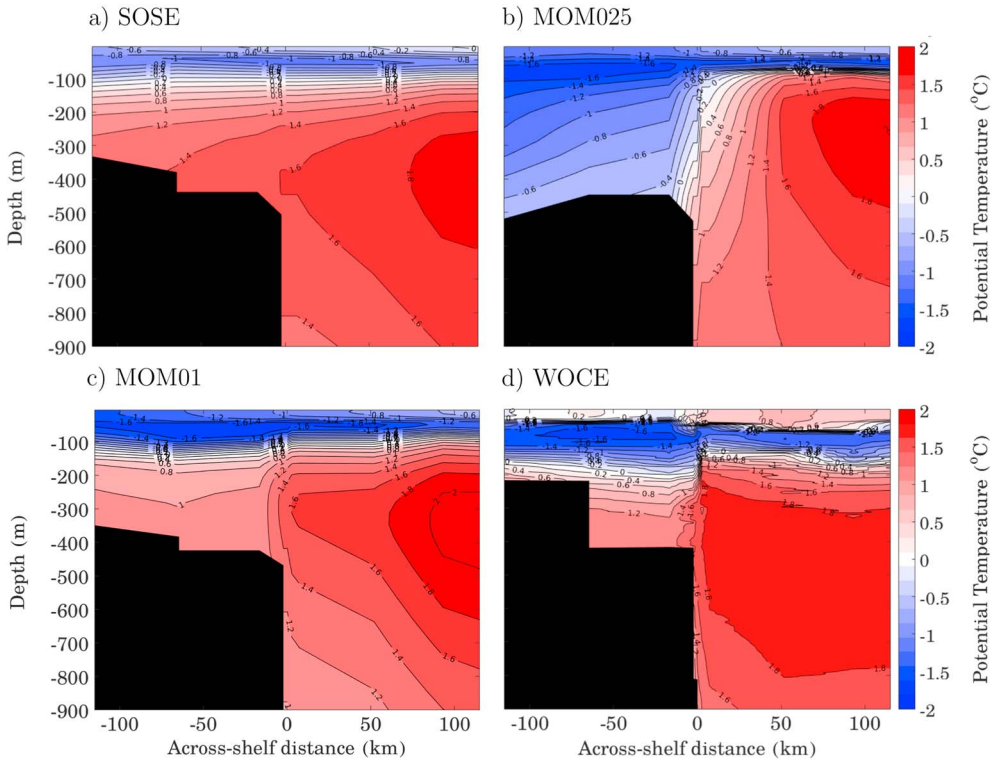

Figure 11. Background temperature sections from (a) SOSE, (b) MOM025, and (c) MOM01 interpolated onto the grid where WOCE S04P line data (d) are available (purple line in Figure 8a). MOM = Modular Ocean Model; SOSE = Southern Ocean State Estimate; WOCE = World Ocean Circulation Experiment.

encouraging, as observational studies suggest that bottom boundary layers are often thicker than the theoretical Ekman layer depth, for example, Wåhlin et al. (2012) and Fer et al. (2016) who observed bottom layer thicknesses of O(100) m on the upper Antarctic continental slope.

5. Discussion and Summary

By calculating temperature anomalies using bottom Ekman layer dynamics and an advection scheme, we have shown that barotropic circulation anomalies, propagated around Antarctica by coastally trapped waves, can cause remote rapid subsurface warming through bottom Ekman transport. We have directly diagnosed the magnitude of the bottom boundary flow/Kelvin wave mechanism of Spence et al. (2017) and shown that if the bottom Ekman layer thickness is increased to 40–70 m on the continental slope (similar increases are supported by observations, e.g., Fer et al., 2016), then the bottom layer temperature anomalies are comparable to that found in the MOM025 and MOM01 simulations. We have also shown that the magnitude of anomalous warming predicted by this mechanism is highly dependent on the climatological temperature field over which the bottom boundary flow advects.

Since warming caused by the advection of isotherms strongly depends on the temperature gradient in the bottom boundary layer, it is worthwhile to compare the model-generated temperature gradients to observations (as opposed to reanalysis products such as SOSE) where available. One of the few hydrographic data sets that contain on-shelf observations along the WAP sector is the S04P line from the World Ocean Circulation Experiment (WOCE; Chipman et al., 2013). We compare our results to the S04P line by interpolating the SOSE, MOM025, and MOM01 temperature fields onto the S04P station positions (indicated in Figure 8a) transecting the WAP slope (Figure 11). This analysis reveals that the cross-slope temperature gradient from WOCE observations is stronger than those produced in MOM01 and SOSE, although it is weaker than MOM025 in the bottom layer. Thus, based on the temperature structure along this WOCE line, we would expect warming produced by the Kelvin wave/bottom Ekman mechanism to be bounded by the MOM025 and MOM01 results. However, our calculation is also affected by a number of other factors that are independent of the static temperature fields. These factors are briefly described here.

As mentioned above, warming due to the Kelvin wave/bottom Ekman mechanism is sensitive to the selection of the effective bottom Ekman layer depth, δ^* (equation (2)), although we showed that a common scaling factor of 10 was able to capture the simulated temperature anomalies in both MOM025 and MOM01. Our calculation also assumes that the along-bottom temperature gradient remains constant. In reality, this gradient will adjust over time due to advection, which could potentially alter the warming rate depending on how the isotherms adjust. If isotherms are shifted away from the slope, then the temperature gradient at the slope will weaken, reducing warming. Seasonality and short time scale variability of the temperature structure may also change the progression of the temperature anomalies. In the model simulations along the WAP, seasonal variability is relatively weak at these depths (not shown), so we suspect its effect would be small in models. However, limited observations suggest that significant submonthly fluctuations in temperature can occur elsewhere, for example, at depth in the Weddell Sea (Graham et al., 2013).

Subsurface warming generated by the Kelvin wave/bottom Ekman mechanism is also sensitive to the wind anomaly imposed. The wind anomaly applied in our calculations (and in Spence et al., 2017) represents an idealized, instantaneous, and time-independent weakening in the coastal easterlies over East Antarctica, modeled on future projections of wind fields around the Antarctic margin. This wind anomaly drives a drop in sea level over the Antarctic continental shelf, forcing a barotropic flow that leads to onshore bottom Ekman transport. If we were to apply a reversal in the anomalous coastal wind direction, noting the uncertainty in future projections of wind fields around the Antarctic margin, this would lead to subsurface cooling under the mechanism described here. We tested the reverse sign (easterly) wind anomaly in the BT model configuration, and as expected, the results were exactly antisymmetric to the westerly wind anomaly experiment. This antisymmetry is unsurprising since the BT model is linear, and we assume a linear response in the bottom Ekman arrest for our diagnostics. Including nonlinearities in the bottom Ekman dynamics may lead to asymmetries between upslope and downslope flow and Ekman arrest times, resulting in a warming or cooling nonlinearity between these two otherwise antisymmetric cases. The sensitivity of the Kelvin wave/bottom Ekman transport mechanism to other variations in wind forcing will be the focus of future work.

The duration of the wind anomaly will also affect the magnitude of subsurface warming produced. For stable wind-driven velocity anomalies, warming will cease after a lag period corresponding to the Ekman arrest time. However, our results do not show warming to cease because the wind-driven velocity anomalies have not yet stabilized after 1 year. We do not consider times longer than 1 year in order to isolate the barotropic effect in the Spence et al. (2017) simulations, which become increasingly unclear over longer times due to confounding interior baroclinic processes.

Our diagnostic calculation considers only one of several possible mechanisms that can drive subsurface warming on the Antarctic continental shelf. We have not considered, for example, changes to the temperature structure due to tides and eddies, ice dynamics and ice-melt feedbacks, or mixing of warmer waters from the bottom boundary layer into the ocean interior. In MOM01, warming concentrated at 108-m depth is significantly larger than the warming simulated along the ocean floor (compare Figures 1b and 1c). This suggests the Kelvin wave/bottom Ekman mechanism is not responsible for all of the shelf water warming seen in MOM01.

Eddies may play an increasingly important role in the on-shelf heat transport of higher resolution models (Graham et al., 2016). Much finer model resolution than we use here is required to resolve the baroclinic radius of deformation on the continental shelf and capture the effects of eddies. Of the two GCMs examined here, the higher resolution model (MOM01) better simulates the observed water mass distributions, although even this model does not resolve the baroclinic radius of deformation south of ~60°S (Hallberg, 2013). However, it should be noted that eddy heat fluxes can be expected to be somewhat weaker in regions of steeply sloping bathymetry, because steep f/H gradients pose a potential vorticity barrier to onshore eddy transport (although troughs in the continental shelf can break this potential vorticity barrier, allowing an alternate pathway for onshore eddy heat transport; Walker et al., 2007). In contrast to on-shelf eddy transport, our mechanism maximizes where the shelf break is steepest (e.g., along the WAP sector, where subsurface temperature anomalies and ice shelf mass loss are also observed to be maximum). This maximization along steep regions of the Antarctic continental slope aligns with the concept of so-called "free modes," which provide a conduit for rapid communication of anomalies around the Antarctic continent along f/H contours (Hughes et al., 1999; Zika et al., 2013). The barotropic velocity fields we produce are consistent with

previous studies wherein low-mode shelf waves, such as barotropic Kelvin waves, dominate large-scale changes in sea level (e.g., Gill & Schumann, 1974).

Beyond its influence on subsurface temperature near the continental slope, the bottom Ekman mechanism discussed here may also contribute to moving heat from the continental slope to the ice shelf front, as the continental shelf is gently sloped and so vertical buoyancy forces will not arrest the flow. However, this contribution may be small compared to other processes, such as lateral advection and mixing, which are not restricted by strong bathymetric gradients on the shelf (unlike over the continental slope). The details of the circulation on the continental shelf and in the vicinity of the ice shelves remains an important area of future research. In particular, the introduction of dynamic ice shelf cavities, not included in our simulations, can create circulation changes that bring strong inflows of warm water under the ice shelves (Jourdain et al., 2017) and may change or amplify the ice shelf mass loss resulting from coastal circulation changes. The interactions between the Kelvin wave/bottom Ekman transport we describe here, and the flow in ice shelf cavities, as well as interactions with the ice shelves themselves, should be the focus of future work.

Lastly, any mode of variability that can influence Antarctic wind stress patterns or SSH anomalies on time scales long enough for a barotropic signal to sufficiently develop (i.e., of order 50 days) may contribute to changing subsurface temperatures around coastal Antarctica via the Kelvin wave/bottom Ekman mechanism. Such modes of variability include ENSO (Ding et al., 2012; Purich et al., 2016; Turner, 2004), the SAM (Thompson et al., 2011), or any feature of the atmospheric circulation that imprints a sustained wind stress anomaly, such as deepening of the Amundsen Sea Low (Hosking et al., 2013; Raphael et al., 2015). For example, during positive ENSO and positive SAM phases, increases in wind forcing near Antarctica drive a largely eastward barotropic change in transport along closed f/H contours (Langlais et al., 2015). This suggests subsurface warming around Antarctica may be enhanced during periods of both positive ENSO and positive SAM phases, due to an increase in bottom boundary layer advection caused by the strengthening of the barotropic flow along f/H contours.

Appendix A: Numerical Estimation of Temperature Anomalies

In this appendix we present the method used to calculate the temperature anomaly due to bottom Ekman advection in equation (14). We assume that the initial state of the anomalous flow, u_{t_0}, will arrest over the time interval $[t_0, t_0 + \tau_0]$. If the flow then changes to $u = u_{t_0} + u_{\Delta t}$ in an interval of Δt, the change in flow, $u_{\Delta t}$, will arrest over the interval $[t_0 + \Delta t, t_0 + \tau_0 + \Delta t]$.

The temperature advection accounting for arrest, $\left(\frac{\partial T}{\partial t}\right)_E^{actual}$, is given by the temperature advection unaffected by arrest, $\left(\frac{\partial T}{\partial t}\right)_E$, minus the same function with a lag of the Ekman arrest time, that is,

$$\left(\frac{\partial T}{\partial t}(\mathbf{x}, t)\right)_E^{actual} = \begin{cases} \left(\frac{\partial T}{\partial t}(\mathbf{x}, t)\right)_E & t \le \tau_0, \\ \left(\frac{\partial T}{\partial t}(\mathbf{x}, t)\right)_E - \left(\frac{\partial T}{\partial t}(\mathbf{x}, t - \tau_0)\right)_E & t > \tau_0. \end{cases} \tag{A1}$$

For numerical approximation, the integral of temperature advection over the infinitesimal time, dt, is replaced by the summation of the instantaneous temperature changes over the discrete time step, Δt, that is,

$$\Delta T(t) = \sum_{i=1}^{M} \Delta T_i, \tag{A2}$$

where $M = t/\Delta t$ and ΔT_i is the temperature change in a single time step. For convergence of equation (A2) we used a time step of $\Delta t = 0.5$ days. Sensitivity to the Ekman arrest time, $\tau_0(x, y)$, makes numerical estimations complex since there will be some regions where $\tau_0 < \Delta t$ and others where $\tau_0 \ge \Delta t$. In steeper regions, τ_0 is only a few hours in contrast to flat bathymetry areas where τ_0 approaches infinity. When the current time, $i\Delta t < \tau_0$, then advection continues and anomalous temperatures will continue to grow until t reaches τ_0. Indeed, even if $i\Delta t > \tau_0$, if there are further changes to the instantaneous barotropic velocity, then the flow will further adjust to these new velocity anomalies, and hence, the temperature advection will change. We denote the temperature advection at the current time as $R(t) \equiv -\bar{\mathbf{u}}'_E \cdot \nabla T$. In order to best approximate the temperature change at the current time t, we consider the following regions.

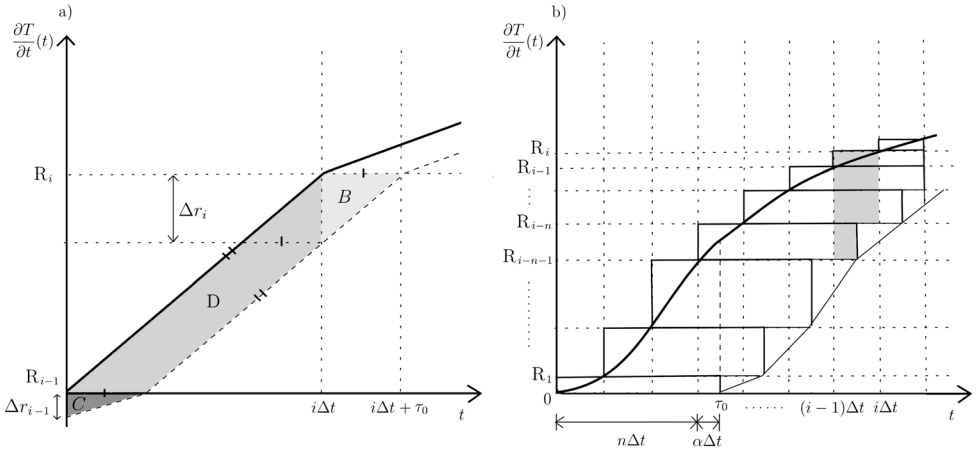

Figure A1. Schematic of temperature advection as a function of time. Solid thick lines represent $R(t)$; shaded regions C and D show the area of integration at the ith time interval, Δt, for (a) $\tau_0 < \Delta t$ and (b) $\Delta t < \tau_0 \leq t_{final}$. In (b), n is the number of whole time intervals within τ_0 with α being the fraction of Δt remaining, such that $\tau_0 = (n + \alpha)\Delta t$.

Where $\tau_0 < \Delta t$, we make the assumption that the change in temperature advection, $\Delta R_i = R_i - R_{i-1}$, over the interval Δt is constant. If Δr_i is the change in temperature advection over a period of τ_0 in the ith time interval (see Figure A1), then the temperature change in the ith interval is given by

$$\Delta T_i = \tau_0 \Delta R_i - \frac{1}{2}\tau_0 \Delta r_i + \frac{1}{2}\tau_0 \Delta r_{i-1}, \tag{A3}$$

$$= \tau_0 \Delta R_i - \frac{\tau_0^2}{2\Delta t}(\Delta R_i - \Delta R_{i-1}), \tag{A4}$$

where we have used similar triangles to find $\Delta r_i = \Delta R_i \tau_0 / \Delta t$ (see Figure A1a; the second and third terms of equation (A2) are the regions denoted by B and C, respectively). This represents the temperature anomaly within each time step, accounting for reductions due to arrested flows. Next, in regions where $\tau_0 \geq \Delta t$, then

$$\Delta T_i = \Delta t \frac{R_i + R_{i-1}}{2}, \tag{A5}$$

that is, the temperature anomaly in these regions is a summation of the average temperature advection over each time interval. Finally, for $i\Delta t > \tau_0 \geq \Delta t$, we let n be the integer number of time intervals in τ_0, and α equal the fractional amount of time intervals remaining, such that $\tau_0 = (n + \alpha)\Delta t$. The temperature anomaly over the ith time interval can then be estimated by

$$\Delta T_i = \Delta t \frac{\Delta R_i}{2} + \Delta t \sum_{j=1}^{\min(i,n-1)} \Delta R_{i-j} + \Delta t \Delta R_{i-\min(i,n)} \left[\alpha + \frac{1}{2}(1-\alpha^2)\right]. \tag{A6}$$

The first term represents the temperature change due to variations in the temperature advection (shaded region in the range (R_{i-1}, R_i) shown in Figure A1b). The second and third terms represent the temperature change due to the preexisting flow that has not yet arrested (shaded regions in range (R_{i-1}, R_n) and (R_n, R_{n-1}) respectively; see Figure A1b).

Acknowledgments
This work was supported by the Australian Research Council, including the ARC Centre of Excellence for Climate System Science (CE110001028). M. H. E. is also supported by the Centre for Southern Hemisphere Oceans Research (CSHOR), a joint research centre between QNLM, CSIRO, UNSW, and UTAS. P. Spence is supported by the ARC DECRA Fellowship DE150100223. Numerical simulations were conducted at the NCI National Facility systems at the Australian National University through the National Computational Merit Allocation Scheme supported by the Australian Government. The model output data are available at https://doi.org/10.25914/5becb179a75cd. The authors would also like to thank Stephen Griffies, Bill Dewer, Jan Zika, and Andy Hogg for insightful discussions.

References

Aoki, S. (2002). Coherent sea level response to the Antarctic oscillation. *Geophysical Research Letters*, *29*(20), 1950. https://doi.org/10.1029/2002GL015733

Brink, K. H., & Lentz, S. J. (2010). Buoyancy arrest and bottom Ekman transport. Part 1: Steady flow. *Journal of Physical Oceanography*, *40*, 621–635. https://doi.org/10.1175/2009JPO4266.1

Carrère, L., & Lyard, F. (2003). Modeling the barotropic response of the global ocean to atmospheric wind and pressure forcing—Comparisons with observations. *Geophysical Research Letters*, *30*(6), 1275. https://doi.org/10.1029/2002GL016473

Chipman, D. W., Takahashi, T., Rubin, S. I., Sutherland, S. C., & Koshlyakov, M. H. (2013). *Partial pressure (or fugacity) of carbon dioxide, dissolved inorganic carbon, temperature, salinity and other variables collected from discrete sample and profile observations using CTD bottle and other instruments from the AKADEMIK IOFFE in the South Pacific Ocean from 1992-02-14 to 1992-04-06 (NODC Accession 0115013)*. Silver Spring, MD: National Oceanographic Data Center, NOAA. Dataset. https://doi.org/10.3334/CDIAC/otg.ndp063

Cossu, R., Wells, M. G., & Wåhlin, A. K. (2010). Influence of the Coriolis force on the velocity structure of gravity currents in straight submarine channel systems. *Journal of Geophysical Research*, *115*, C11016. https://doi.org/10.1029/2010JC006208

DeConto, R. M., & Pollard, D. (2016). Contribution of Antarctica to past and future sea-level rise. *Nature*, *531*, 591–597. https://doi.org/10.1038/nature17145

Depoorter, M. A., Bamber, J. L., Griggs, J. A., Lenaerts, J. T. M., Ligtenberg, S. R. M., van den Broeke, M. R., & Moholdt, G. (2013). Calving fluxes and basal melt rates of Antarctic ice shelves. *Nature*, *502*, 89–92. https://doi.org/10.1038/nature12567

Ding, Q., Steig, E. J., Battisti, D. S., & Wallace, J. M. (2012). Influence of the tropics on the southern annular mode. *Journal of Climate*, *25*, 6330–6348. https://doi.org/10.1175/JCLI-D-11-00523.1

Fer, I., Darelius, E., & Daae, K. B. (2016). Observations of energetic turbulence on the Weddell Sea continental slope. *Geophysical Research Letters*, *43*, 760–766. https://doi.org/10.1002/2015GL067349

Flexas, M. M., Schodlok, M. P., Padman, L., Menemenlis, D., & Orsi, A. H. (2015). Role of tides on the formation of the Antarctic Slope Front at the Weddell-Scotia Confluence. *Journal of Geophysical Research: Oceans*, *120*, 3658–3680. https://doi.org/10.1002/2014JC010372

Frankcombe, L. M., Spence, P., Hogg, A. M., England, M. H., & Griffies, S. M. (2013). Sea level changes forced by Southern Ocean winds. *Geophysical Research Letters*, *40*, 5710–5715. https://doi.org/10.1002/2013GL058104

Garrett, C., MacCready, P., & Rhines, P. (1993). Boundary mixing and arrested Ekman layers: Rotating stratified flow near a sloping boundary. *Annual Review of Fluid Mechanics*, *25*, 291–323.

Gill, A. E., & Clarke, A. J. (1974). Wind-induced upwelling, coastal currents and sea-level changes. *Deep-Sea Research*, *21*, 325–345.

Gill, A. E., & Schumann, E. H. (1974). The generation of long shelf waves by the wind. *Journal of Physical Oceanography*, *4*, 83–90.

Graham, J. A., Dinniman, M. S., & Klinck, J. M. (2016). Impact of model resolution for on-shelf heat transport along the west antarctic peninsula. *Journal of Geophysical Research: Oceans*, *121*, 7880–7897. https://doi.org/10.1002/2016JC011875

Graham, J. A., Heywood, K. J., Holland, P. R., & Chavanne, C. P. (2013). Seasonal variability of water masses and transport on the Antarctic continental shelf and slope in the southeastern Weddell Sea. *Journal of Geophysical Research: Oceans*, *118*, 2201–2214. https://doi.org/10.1002/jgrc.20174

Griffies, S. M. (2016). Elements of the Modular Ocean Model (MOM) (*GFDL Ocean Group Tech. Rep. 7*). Princeton, NJ: NOAA/GFDL. Retrieved from http://www.mom-ocean.org/web/docs

Hallberg, R. (2013). Using a resolution function to regulate parameterizations of oceanic mesoscale eddy fields. *Ocean Modelling*, *72*, 92–103.

Harig, C., & Simon, F. (2015). Accelerated West Antarctic ice mass loss continues to outpace antarctic gains. *Earth and Planetary Science Letters*, *415*, 131–141.

Hellmer, H. H., Kauker, F., Timmermann, R., Determann, J., & Rae, J. (2012). Twenty-first-century warming of a large Antarctic ice-shelf cavity by a redirected coastal current. *Nature*, *485*, 225–228. https://doi.org/10.1038/nature11064

Holland, P. R., Jenkins, A., & Holland, D. M. (2008). The response of ice shelf basal melting to variations in ocean temperature. *Journal of Climate*, *21*(11), 2558–2572. https://doi.org/10.1175/2007JCLI1909.1

Hosking, J. S., Orr, A., Marshall, G. J., Turner, J., & Phillips, T. (2013). The influence of the Amundsen-Bellingshausen seas low on the climate of West Antarctica and its representation in coupled climate model simulations. *Journal of Climate*, *26*, 6633–6648. https://doi.org/10.1175/JCLI-D-12-00813.1

Hughes, C. W., Meredith, M. P., & Heywood, K. J. (1999). Wind-driven transport fluctuations through Drake Passage: A southern mode. *Journal of Physical Oceanography*, *29*, 1971–1992.

Jacobs, S. S. (1991). On the nature and significance of the Antarctic slope front. *Marine Chemistry*, *35*, 9–24.

Jenkins, A., Dutrieux, P., Jacobs, S. S., McPhail, S. D., Perrett, J. R., Webb, A. T., & White, D. (2010). Observations beneath pine island glacier in West Antarctica and implications for its retreat. *Nature Geoscience*, *3*, 468–472.

Jourdain, N., Mathiot, P., Merino, N., Durand, G., Le Sommer, J., Spence, P., et al. (2017). Ocean circulation and sea ice thinning induced by melting ice shelves in the Amundsen Sea. *Journal of Geophysical Research: Oceans*, *122*, 2550–2573. https://doi.org/1002/2016JC012509

Kimura, S., Jenkins, A., Regan, H., Holland, P. R., Assmann, K. M., Whitt, D. B., et al. (2017). Oceanographic controls on the variability of ice-shelf basal melting and circulation of glacial meltwater in the Amundsen Sea Embayment. *Journal of Geophysical Research: Oceans*, *122*, 10,131–10,155. https://doi.org/10.1002/2017JC012926

Klinck, J. M., & Dinniman, M. S. (2010). Exchange across the shelf break at high southern latitudes. *Ocean Science*, *6*, 513–524. https://doi.org/10.5194/os-6-513-2010

Kusahara, K., & Ohshima, K. I. (2014). Kelvin waves around Antarctica. *Journal of Physical Oceanography*, *44*, 2909–2920. https://doi.org/10.1175/JPO-D-14-0051.1

Langlais, C. E., Rintoul, S. R., & Zika, J. D. (2015). Sensitivity of Antarctic Circumpolar Current transport and eddy activity to wind patterns in the Southern Ocean. *Journal of Physical Oceanography*, *45*, 1051–1067. https://doi.org/10.1175/JPO-D-14-0053.1

MacCready, P., & Rhines, P. B. (1991). Buoyant inhibition of Ekman transport on a slope and its effect on stratified spin-up. *Journal of Fluid Mechanics*, *223*, 631–661.

MacCready, P., & Rhines, P. B. (1993). Slippery bottom boundary layers on a slope. *Journal of Physical Oceanography*, *23*, 5–22.

Mazloff, M. R., Heimbach, P., & Wunsch, C. (2010). An eddy-permitting Southern Ocean state estimate. *Journal of Physical Oceanography*, *40*, 880–899.

Middleton, J. H., Foster, T. D., & Foldvik, A. (1982). Low-frequency currents and continental shelf waves in the southern Weddell Sea. *Journal of Physical Oceanography*, *12*, 618–634.

Nitsche, F. O., Porter, D., Williams, G., Cougnon, E. A., Fraser, A. D., Correia, R., & Guerrero, R. (2017). Bathymetric control of warm ocean water access along the east Antarctic margin. *Geophysical Research Letters*, *44*, 8936–8944. https://doi.org/10.1002/2017GL074433

Pritchard, H. D., Ligtenberg, S. R. M., Fricker, H. A., Vaughan, D. G., van der Broeke, M. R., & Padmen, L. (2012). Antarctic ice-sheet loss driven by basal melting of ice shelves. *Nature*, *484*, 502–505. https://doi.org/10.1038/nature10968

Purich, A., England, M. H., Cai, W., Chikamoto, Y., Timmermann, A., Fyfe, J. C., et al. (2016). Tropical Pacific SST drivers of recent Antarctic sea ice trends. *Journal of Climate*, *29*, 8931–8948. https://doi.org/10.1175/JCLI-D-16-0440.1

Raphael, M. N., Marshall, G. J., Turner, J., Fogt, R. L., Schneider, D., Dixon, D. A., et al. (2015). The Amundsen Sea low variability, change, and impact on Antarctic climate. *Bulletin of the American Meteorological Society*, *97*, 111–121. https://doi.org/10.1175/BAMS-D-14-00018.1

Rignot, E., Vaughan, D. G., Schmeltz, M., Dupont, T., & MacAyeal, D. (2002). Acceleration of Pine Island and Thwaites Glaciers, West Antarctica. *Annals of Glaciology*, *34*, 189–194. https://doi.org/10.3189/172756402781817950

Robertson, R. (2013). Tidally induced increases in melting of Amundsen Sea ice shelves. *Journal of Geophysical Research: Oceans*, *118*, 3138–3145. https://doi.org/10.1002/jgrc.20236

Rodriguez, A. R., Mazloff, M. R., & Gille, S. T. (2016). An oceanic heat transport pathway to the Amundsen Sea Embayment. *Journal of Geophysical Research: Oceans*, *121*, 3337–3349. https://doi.org/10.1002/2015JC011402

Schmidtko, S., Heywood, K. J., Thompson, A. F., & Aoki, S. (2014). Multidecadal warming of Antarctic waters. *Science*, *346*, 1227–1231. https://doi.org/10.1126/science.1256117

Shchepetkin, A. F., & McWilliams, J. C. (2005). The Regional Ocean Modeling System (ROMS): A split-explicit, free-surface, topography-following coordinate ocean model. *Ocean Modelling*, *9*, 347–404.

Spence, P., Griffies, S. M., England, M. H., Hogg, A. M., Saenko, O. A., & Jourdain, N. C. (2014). Rapid subsurface warming and circulation changes of Antarctic coastal waters by poleward shifting winds. *Geophysical Research Letters*, *41*, 4601–4610. https://doi.org/10.1002/2014GL060613

Spence, P., Holmes, R. M., Hogg, A. M., Griffies, S. M., Stewart, K. D., & England, M. H. (2017). Localized rapid warming of West Antarctic subsurface waters by remote winds. *Nature Climate Change*, *7*, 595–603. https://doi.org/10.1038/nclimate3335

St-Laurent, P., Klinck, J. M., & Dinniman, M. S. (2013). On the role of coastal troughs in the circulation of Warm Circumpolar Deep Water on Antarctic Shelves. *Journal of Physical Oceanography*, *43*, 51–64. https://doi.org/10.1175/JPO-D-11-0237.1

Stewart, A. L., & Thompson, A. F. (2015). Eddy-mediated transport of Warm Circumpolar Deep Water across the Antarctic shelf break. *Geophysical Research Letters*, *42*, 432–440. https://doi.org/0.1002/2014GL062281

Thompson, D. W. J., & Solomon, S. (2002). Interpretation of recent Southern Hemisphere climate change. *Science*, *296*, 895–899.

Thompson, D. W. J., Solomon, S., Kushner, P. J., England, M. H., Grise, K. M., & Karoly, D. J. (2011). Signatures of the Antarctic ozone hole in Southern Hemisphere surface climate change. *Nature Geoscience*, *4*, 741–749.

Turner, J. (2004). The El Nino-Southern Oscillation and Antarctica. *International Journal of Climatology*, *24*, 1–31. https://doi.org/10.1002/joc.965

Walker, D. P., Brandon, M. A., Jenkins, A., Allen, J. T., Dowdeswell, J. A., & Evans, J. (2007). Oceanic heat transport onto the Amundsen Sea shelf through a submarine glacial trough. *Geophysical Research Letters*, *34*, L02602. https://doi.org/10.1029/2006GL028154

Wåhlin, A. K., Muench, R. D., Arneborg, L., Björk, G., Ha, H. K., Lee, S. H., & Alsén, H. (2012). Some implications of Ekman layer dynamics for cross-shelf exchange in the Amundsen Sea. *Journal of Physical Oceanography*, *42*, 1461–1474. https://doi.org/10.1175/JPO-D-11-041.1

Wåhlin, A. K., & Walin, G. (2001). Downward migration of dense bottom currents. *Environmental Fluid Mechanics*, *1*, 257–279. https://doi.org/10.1023/A:1011520432200

Zika, J. D., Sommer, J. L., Dufour, C. O., Naveria-Garabato, A., & Blaker, A. (2013). Acceleration of the Antarctic Circumpolar Current by wind stress along the Coast of Antarctica. *Journal of Physical Oceanography*, *43*, 2772–2784. https://doi.org/10.1175/JPO-D-13-091.1